Noname manuscript No.
(will be inserted by the editor)

Non-normal Mode Onset of Convection in a Vertical Porous Cylinder

Peder A. Tyvand · Jonas Kristiansen Nøland

Received: date / Accepted: date

Abstract This is the first study reporting a full three-dimensional (3D) non-normal-mode onset of convection in a porous medium. In this paper, the onset of thermal convection in a vertical porous cylinder is investigated theoretically. In particular, the contribution includes the following novelties. The homogeneous cylinder has a circular cross-section. The eigenvalue problem is non-separable in space because of a constant heat flux condition at the upper boundary. In addition, a partly conducting cylinder wall is represented by a Robin parameter a. All boundaries are impermeable. The eigenvalue problem is solved numerically in the COMSOL Multiphysics environment. The critical Rayleigh number for the lowest onset modes are reported as a function of the ratio of the cylinder radius and its height. The only mode-number, m, represents azimuthal dependency. The axisymmetric mode $m = 0$ corresponds to the preferred mode of convection for a small-cylinder radii. The numerical onset criterion is validated with the well-known analytical limit case, $a \to \infty$. Finally, we performed a visual comparison of the thermo-mechanical eigenfunctions against an established problem, where the only difference is the thermal condition at the upper boundary. The present 3D analysis is a step towards a full adequate modeling of experimental reality for convection onset, beyond the standard constraints of mathematical convenience.

Keywords Convection · Onset · Non-normal-modes · Porous cylinder

P. A. Tyvand
Faculty of Mathematical Sciences and Technology
Norwegian University of Life Sciences
1432 Ås, Norway
Tel.: +47-67231564
E-mail: Peder.Tyvand@nmbu.no

J. K. Nøland (Corresponding Author)
Faculty of Information Technology and Electrical Engineering
Norwegian University of Science and Technology
E-mail: Jonas.K.Noland@ntnu.no

1 Introduction

The onset of convection in a horizontal porous layer heated from below was first investigated in two pioneering papers [1], [2]. The lower and upper boundary were assumed impermeable and thermally conducting, leading to normal-mode type eigenfunctions in the vertical direction. With infinite horizontal extent, a Fourier decomposition in the horizontal direction implies normal-mode dependency. Beck [3] generalized the original theory to a rectangular porous cavity with impermeable and thermally insulating walls, which preserves the normal-mode type of solution in the horizontal directions.

Tyvand and Storesletten [4] pointed out that normal modes in a spatial direction represent a degeneracy of the eigenvalue problem, reducing it from a fourth-order problem to an essentially second-order problem. While Wooding [5] had shown how normal modes could be applied to the onset problem for any vertical cylinder with insulating and impermeable cylinder walls, his analysis was confirmed and extended in [4].

Vertical cylinders are the only class of three-dimensional (3D) porous cavities where the onset modes for convection can be composed by normal modes, because of the lack of curvature in a vertical cross-section. If a porous cavity has a vertical cross-section with curved or sloping boundary, normal modes can no longer constitute the eigenfunctions. It implies that normal modes are not available for solving an onset problem in 3D porous cavities other than vertical cylinders.

Convection in a horizontal circular cylinder was investigated by Storesletten and Tveitereid [6]. The 2D version of their theory was generalized to arbitrary cross-sections by Rees and Tyvand [7], who discovered that the onset problem for a 2D porous cavity could be solved by a Helmholtz equation when the cavity has thermally conducting and impermeable walls. Normal modes will then contribute to the eigenfunctions, but only after a horizontal Fourier component has been separated out. This separation takes care of a horizontal phase shift of a quarter of a wavelength between the eigenfunctions for the temperature and stream-function. This phase shift applies to internal isolines for temperature versus stream-function, while these isolines have no mutual phase shift at the exterior boundary. The degeneracy of such eigenvalue problems makes any set of temperature and stream-function eigenfunctions interchangeable. These nice properties of thermo-mechanical eigenfunctions, discovered in [7], apply only 2D cavities.

The present work contains a full 3D analysis. It is the first study of non-normal modes for the onset of convection in a vertical cylinder heated from below. The starting point for developing the present model is our recent work [8] with steady non-normal modes for convection onset in a porous rectangle. This previous work involved one single corner where the thermo-mechanical eigenfunctions are non-analytical, defying local Taylor expansions, but with locally analytical eigenfunctions around the three other corners. We take the 2D geometry of our first non-normal mode paper [8] and make it 3D by generating axisymmetry by revolving the 2D cross-section around the vertical z

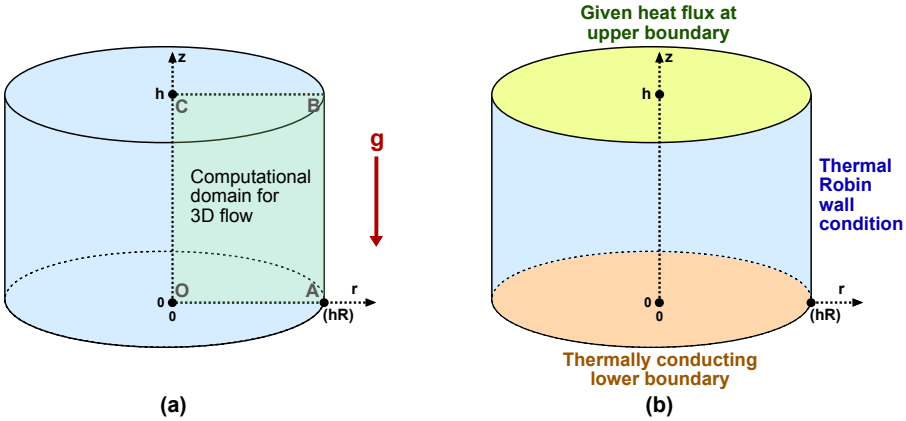

Fig. 1 Perspective 3D sketch of the vertical porous cylinder. The length unit is the height h of the cylinder. The horizontal cross-section is circular, with a dimensionless radius R. The direction of gravity is indicated. (a) Geometric configuration with 2D computational domain for the 3D flow. The eigenvalue problem is to be formulated in the vertical half cross-section $OABC$. (b) The chosen thermal boundary conditions. All boundaries are assumed impermeable.

axis. Thereby we arrive at only one thermo-mechanical boundary for the horizontal direction, which is a mathematical simplification in comparison with the previous 2D geometry [8].

The present non-degenerate onset problem for a 3D cylinder contrasts previous work summarized in [4], where the spatial dependencies separate due to normal modes either horizontally or vertically. We will investigate the qualitative and quantitative effects of this full fourth-order eigenvalue problem.

The remainder of the paper is organized as follows. Section 2 formulates the problem mathematically from first principles. Then, the eigenvalue problem is described in Section 3. In Section 4, the numerical results for the conducting cylinder wall are presented. The results are validated against well-knows analytical solutions in Section 5. A qualitative comparison is also made in Section 6, where one thermal condition is modified. Finally, Section 7 summarizes and concludes the paper.

2 Mathematical formulation

A three-dimensional porous medium is bounded by horizontal planes $z = 0$ and $z = h$. The porous medium is homogeneous and isotropic. Cartesian coordinates (x, y, z) are introduced. The z axis is directed vertically upwards. We will consider a vertical circular cylinder, noting that the linear theory has been established both for impermeable insulating walls (Wooding [5]), and for open conducting walls (Barletta and Storesletten [9]).

The velocity vector $\mathbf{v}$ has Cartesian components (u, v, w). The temperature field is represented as $T(x, y, z, t)$ with t denoting time. In the undisturbed

state, the lower plane $z = 0$ is kept at a constant temperature $T = T_0$. The upper plane $z = h$ has a given temperature gradient $-\beta$. Here β is positive. The heat flux is thus given through the impermeable upper boundary. The gravitational acceleration g is written in vector form as $\mathbf{g}$.

The standard Darcy-Boussinesq equations for free thermal convection in a porous medium can be written

$$\nabla P + \frac{\mu}{K}\mathbf{v} + \rho_0 \alpha \ (T - T_0)\mathbf{g} = 0, \tag{1}$$

$$\nabla \cdot \mathbf{v} = 0, \tag{2}$$

$$(\rho c_p)_m \frac{\partial T}{\partial t} + (\rho c_p)_f \ \mathbf{v} \cdot \nabla T = \lambda_m \nabla^2 T. \tag{3}$$

In these equations, P is the dynamic pressure, α is the coefficient of thermal expansion, $\rho = \rho_0$ is the fluid density at the reference temperature T_0, μ is the dynamic viscosity of the saturating fluid, K is the permeability, c_p is the specific heat at constant pressure, and λ_m is the thermal conductivity of the saturated porous medium. The subscript m refers here to an average over the solid/fluid mixture, while the subscript f refers to the saturating fluid alone.

The lower and upper boundaries support a given temperature gradient β across the porous layer. The undisturbed basic state of pure conduction has a given temperature at the lower boundary

$$T = T_0 + \Delta T, \quad \text{at} \quad z = 0, \tag{4}$$

while the temperature gradient is given at the upper boundary

$$\frac{\partial T}{\partial z} = -\beta, \quad \text{at} \quad z = h. \tag{5}$$

The temperature difference in the undisturbed state is $\Delta T = \beta h$, and T_0 is a reference temperature. This basic state is to be disturbed with infinitesimal perturbations.

The kinematic conditions for the impermeable lower and upper boundaries are

$$w = 0, \quad \text{at} \quad z = 0, \tag{6}$$

$$w = 0, \quad \text{at} \quad z = h. \tag{7}$$

Figure 1 shows a definition sketch for the vertical porous cylinder with circular cross-section. The direction of gravity is indicated. A vertical half cross-section $OABC$ is depicted. This is the domain of computation for the eigenvalue problem.

2.1 Dimensionless equations

From now on we work with dimensionless variables. The length unit is the height of the vertical cylinder, and the dimensionless radius of its circular cross-section is denoted by R. We reformulate the mathematical problem in dimensionless form by means of the transformations

$$\begin{aligned} &\frac{1}{h}(x,z) \to (x,z), \qquad \frac{h}{\kappa_m}(u,v,w) \to (u,v,w), \qquad h\nabla \to \nabla, \\ &\frac{1}{\Delta T}(T-T_0) \to T, \qquad \frac{K}{\mu\kappa_m}(P-P_0) \to P, \qquad \frac{(\rho c_p)_f \kappa_m}{(\rho c_p)_m h^2} t \to t, \end{aligned} \tag{8}$$

where $\kappa_m = \lambda_m/(\rho_0 c_p)_f$ is the thermal diffusivity of the saturated porous medium. We denote the vertical unit vector by $\mathbf{k}$, directed upwards.

The dimensionless governing equations can then be written

$$\mathbf{v} + \nabla P - RaT\mathbf{k} = 0. \tag{9}$$

$$\nabla \cdot \mathbf{v} = 0 \tag{10}$$

$$\frac{\partial T}{\partial t} + \mathbf{v} \cdot \nabla T = \nabla^2 T, \tag{11}$$

with the boundary conditions of impermeable and conducting lower plane

$$w = T - 1 = 0, \quad z = 0, \tag{12}$$

and impermeable upper plane with a negative unit temperature gradient

$$w = \frac{\partial T}{\partial z} + 1 = 0, \quad z = 1. \tag{13}$$

The Rayleigh number Ra is defined as

$$Ra = \frac{\rho_0 g \alpha K \beta h^2}{\mu \kappa_m}. \tag{14}$$

2.2 Basic solution

The stationary basic solution of eqs. (9)-(13) is given subscript "b".

$$\mathbf{v}_b = 0, \quad T_b = 1 - z, \quad P_b = Ra\ z\left(1 - \frac{z}{2}\right). \tag{15}$$

This basic state has a linear temperature profile.

2.3 Linearized perturbation equations

In our stability analysis we disturb the basic state (15) with perturbed fields

$$\mathbf{v} = \mathbf{v}_b + \mathbf{v}, \quad T = T_b(z) + \Theta, \quad P = P_b(z) + p. \tag{16}$$

where the perturbations $\mathbf{v}$, Θ, p are functions of x, y, z and t. Linearizing eqs. (9)-(11) with respect to perturbations and eliminating the pressure gives

$$\nabla^2 w = Ra \nabla_1^2 \Theta, \tag{17}$$

$$\frac{\partial \Theta}{\partial t} - w = \nabla^2 \Theta. \tag{18}$$

In eq. (17), we introduce the horizontal Laplacian operator $\nabla_1^2 = \partial^2/\partial x^2 + \partial^2/\partial y^2$. Since the vertical component of the vorticity is zero, and the flow is incompressible, one single scalar function $\Psi(x, y, z)$ is sufficient for representing the entire 3D thermo-mechanical vector field. The velocity field is

$$\mathbf{v} = \nabla \times (\nabla \times \mathbf{k}\Psi), \tag{19}$$

where $\mathbf{k}$ is the unit vector in the vertical direction. The components of this vectorial relationship are

$$(u, v, w) = \left(\frac{\partial^2 \Psi}{\partial x \partial z}, \frac{\partial^2 \Psi}{\partial y \partial z}, -\nabla_1^2 \Psi \right). \tag{20}$$

Inserting $w = -\nabla_1^2 \Psi$ in eq. (17) leads to the conclusion that the perturbation temperature is given by

$$\Theta = -Ra^{-1} \nabla^2 \Psi, \tag{21}$$

after having integrated out the common 2D Laplace operator on each side of the resulting vorticity equation. This can be done because the 2D Laplace equation has only a trivial solution with homogeneous boundary condition.

The heat equation (18) becomes

$$\nabla_1^2 \Psi = \nabla^2 \Theta - \frac{\partial \Theta}{\partial t}. \tag{22}$$

2.4 Governing equations in cylinder coordinates

We will formulate the problem in the cylinder coordinates (r, ϕ, z) where the coordinates in the horizontal plane are defined as

$$r = \sqrt{x^2 + y^2}, \quad \phi = \arctan\left(\frac{y}{x}\right). \tag{23}$$

The velocity vector in cylinder coordinates has the components (v_r, v_ϕ, w), which are defined by

$$(v_r, v_\phi, w) = \left(\frac{\partial^2 \Psi}{\partial r \partial z}, \frac{1}{r} \frac{\partial^2 \Psi}{\partial \phi \partial z}, -\nabla_1^2 \Psi \right). \tag{24}$$

We can reformulate the governing equations by introducing the versions in cylinder coordinates of the Laplacian operators ∇_1^2 and ∇^2, where

$$\nabla_1^2\Psi = \frac{1}{r}\frac{\partial}{\partial r}\left(r\frac{\partial\Psi}{\partial r}\right) + \frac{1}{r^2}\frac{\partial^2\Psi}{\partial\phi^2}, \qquad \nabla^2\Psi = \nabla_1^2\Psi + \frac{\partial^2\Psi}{\partial z^2}. \tag{25}$$

The governing equations are now expressed in cylinder coordinates as

$$Ra\ \Theta + \frac{1}{r}\frac{\partial}{\partial r}\left(r\frac{\partial\Psi}{\partial r}\right) + \frac{1}{r^2}\frac{\partial^2\Psi}{\partial\phi^2} + \frac{\partial^2\Psi}{\partial z^2} = 0, \tag{26}$$

$$\frac{1}{r}\frac{\partial}{\partial r}\left(r\frac{\partial\Psi}{\partial r}\right) + \frac{1}{r^2}\frac{\partial^2\Psi}{\partial\phi^2} = \frac{1}{r}\frac{\partial}{\partial r}\left(r\frac{\partial\Theta}{\partial r}\right) + \frac{1}{r^2}\frac{\partial^2\Theta}{\partial\phi^2} + \frac{\partial^2\Theta}{\partial z^2} - \frac{\partial\Theta}{\partial t}. \tag{27}$$

2.5 Boundary conditions at the cylinder wall

We will now introduce a choice of thermo-mechanical conditions at the vertical cylinder walls. As thermal boundary condition we take a general Robin condition

$$\Theta + a\ \mathbf{n}\cdot\nabla\Theta = 0, \quad \text{at the cylinder contour,} \tag{28}$$

where $a \geq 0$ is a dimensionless parameter of partial conduction. This condition was derived by Nygård and Tyvand [10], assuming that there is a thin cylindrical layer separating the thermoconvective flow domain of the porous cylinder from a surrounding medium that is perfectly conducting. As kinematic condition we take the simple condition of impermeable walls

$$\mathbf{n}\cdot\mathbf{v} = 0, \quad \text{at the cylinder contour,} \tag{29}$$

where $\mathbf{n}$ is the horizontal unit normal vector on the cylinder surface, pointing out from the porous cylinder.

3 The eigenvalue problem in the vertical r, z plane

We will formulate the eigenvalue problem in the vertical r, z plane. We introduce the dimensionless radius R of the circular cross-section of the cylinder. We separate out the tangential ϕ dependency as follows

$$\Psi = \psi(r,z)e^{im\phi}e^{\sigma t}, \quad \Theta = \theta(r,z)e^{im\phi}e^{\sigma t}. \tag{30}$$

We have introduced the exponential growth factor $\sigma = \sigma_r + i\sigma_i$, where i is the imaginary unit. Marginal stability is defined by $\sigma_r = 0$. We assume that $\sigma_i = 0$, after having performed some computations which confirm that the onset mode is non-oscillatory.

For each given azimuthal mode number ($m = 0, 1, 2, 3, ..$) we thus have a set of eigenfunctions $\psi = \psi_m(r,z)$ and $\theta = \theta_m(r,z)$. The governing equations

are now formulated with a subscript $m = 0, 1, 2, ..$ representing the azimuthal mode for each eigenfunction

$$Ra\ \theta_m + \frac{1}{r}\frac{\partial}{\partial r}\left(r\frac{\partial \psi_m}{\partial r}\right) - \frac{m^2}{r^2}\psi_m + \frac{\partial^2 \psi_m}{\partial z^2} = 0, \tag{31}$$

$$\frac{1}{r}\frac{\partial}{\partial r}\left(r\frac{\partial \psi_m}{\partial r}\right) - \frac{m^2}{r^2}\psi_m = \frac{1}{r}\frac{\partial}{\partial r}\left(r\frac{\partial \theta_m}{\partial r}\right) - \frac{m^2}{r^2}\theta_m + \frac{\partial^2 \theta_m}{\partial z^2}, \tag{32}$$

Insertion of eq. (31) into eq. (32) yields

$$-\frac{\partial^2 \psi_m}{\partial z^2} - Ra\ \theta_m = \frac{1}{r}\frac{\partial}{\partial r}\left(r\frac{\partial \theta_m}{\partial r}\right) - \frac{m^2}{r^2}\theta_m + \frac{\partial^2 \theta_m}{\partial z^2}, \tag{33}$$

which makes the Rayleigh number appear in both the vorticity equation and the heat equation. This is beneficial for the numerical stability. We introduce the azimuthal mode number m in eq. (25) and reformulate the horizontal Laplacian

$$\nabla_1^2 \psi_m = \frac{1}{r}\frac{\partial}{\partial r}\left(r\frac{\partial \psi_m}{\partial r}\right) - \frac{m^2}{r^2}\psi_m, \tag{34}$$

We formulate the boundary conditions. At the lower boundary we have

$$\theta_m = \psi_m = 0, \quad z = 0, \tag{35}$$

and at the upper boundary

$$\frac{\partial \theta_m}{\partial z} = \psi_m = 0, \quad z = 1. \tag{36}$$

As boundary conditions at the cylinder wall we take a Robin-type thermal condition (28) rewritten as

$$\theta_m + a\ \frac{\partial \theta_m}{\partial r} = 0, \quad r = R, \tag{37}$$

while the kinematic condition of an impermeable cylinder wall (29) takes the form

$$\frac{\partial \psi_m}{\partial r} = 0, \quad r = R. \tag{38}$$

Note that the radial derivative of the 3D scalar function ψ_m expresses that the outer boundary is a streamline, different from the similar condition for a 2D streamfunction.

The Robin parameter a is a non-negative number representing partial conduction. The lower limit $a = 0$ is the case of conducting cylinder wall, studied by Haugen and Tyvand [11] in the presence of normal modes in the vertical direction, where the thermal condition of the upper boundary differs from the present one.

The asymptotic limit $a \to \infty$ for the Robin parameter is the case of an insulating cylinder wall. This case will serve as our benchmarking case, and it has been studied by Wang [12].

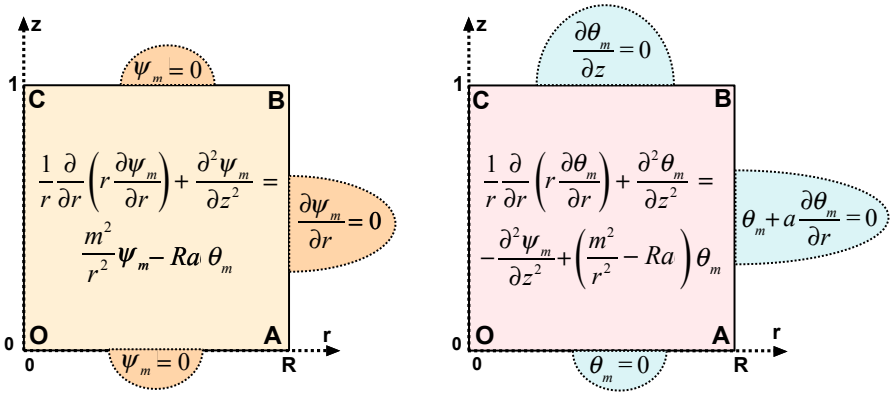

Fig. 2 Sketches of the vertical half cross-section plane $OABC$ shown in Fig. 1, including boundary conditions and governing equations.

Axisymmetry is represented by the lowest azimuthal mode number $m = 0$. Our general theory includes non-axisymmmetric modes with the integer parameter $m > 0$, which is the azimuthal mode number. Haugen and Tyvand [11] found that the axisymmetric mode is preferred for all aspects ratios when the cylinder wall is conducting, but this will not be the case for the present model.

The concept of streamlines applies only to the axisymmetric case. For fully 3D flows, there will be stagnation points in the vertical plane, also for non-axisymmetric flows ($m \geq 1$). According to eq. (24) these stagnation points are given by

$$e^{-im\phi}(v_r, w) = \left(\frac{\partial^2 \psi_m}{\partial r \partial z}, -\frac{1}{r}\frac{\partial}{\partial r}\left(r\frac{\partial \psi_m}{\partial r}\right) + \frac{m^2}{r^2}\psi_m\right) = (0,0). \tag{39}$$

Figure 2 illustrates the general eigenvalue problem in the half cross section plane $OABC$ that we have introduced in *Figure* 1. The 3D eigenvalue problem is formulated in the r, z plane, even if it is not an axisymmetric problem. This is because the azimuthal mode number m is separated out. Note that the Rayleigh number is directly effecting both equations in the model (eqs. 31 and 32 modified for numerical stability).

3.1 The Stokes stream function for axisymmetric flow

The flow field can be visualized by streamlines for the axisymmetric case $m = 0$, by introducing the Stokes stream function $\chi(r, z)$ which we define by

$$v_r = \frac{1}{r}\frac{\partial \chi}{\partial z}, \quad w = -\frac{1}{r}\frac{\partial \chi}{\partial r}, \tag{40}$$

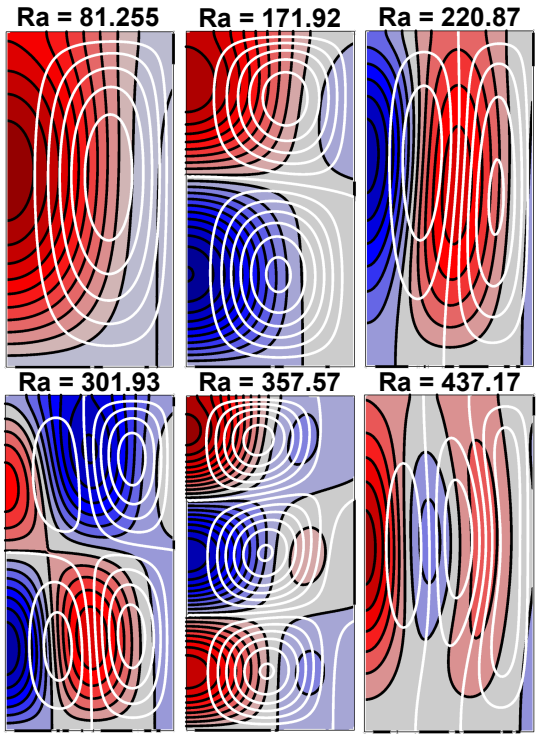

Fig. 3 Axisymmetric eigenfunction plots ($m = 0$) for a slender cylinder ($R = 0.5$). Black lines and coloring represent isotherms, while white lines are streamlines. Conducting cylinder wall ($a = 0$).

and thereby we can link $\chi(r, z)$ to the axisymmetric polodial vector potential $\psi(r, z)$ as follows

$$\chi = r\frac{\partial \psi}{\partial r}. \tag{41}$$

The axisymmetric streamlines are then represented by the set of isolines $\chi(r, z) = constant$ in the r, z plane. This computation of streamlines is limited to the axisymmetric modes $m = 0$.

4 Numerical results for conducting cylinder wall ($a = 0$)

We will show numerical solutions of the thermo-mechanical eigenvalue problem, based on the commercial finite-element environment of COMSOL Multiphysics. The following plots for the eigenfunctions represent the half cross-section $OABC$ shown in *Figure* 1, where the left-hand side of each figure follows the vertical z axis, where $r = 0$.

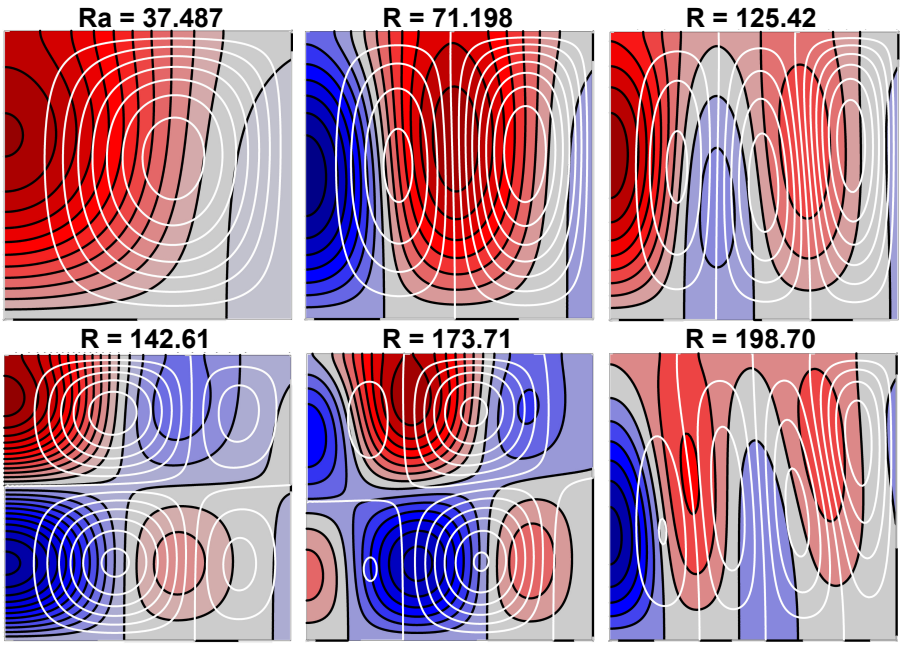

Fig. 4 Axisymmetric eigenfunction plots ($m = 0$) for a cylinder with dimensionless radius $R = 1$. Black lines and coloring represent isotherms, while white lines are streamlines. Conducting cylinder wall ($a = 0$).

4.1 Axisymmetric mode ($m = 0$)

We start with displaying the results for the axisymmetric mode $m = 0$. Axisymmetry is required in order to be able to plot streamlines, which provide a broader understanding of the eigenfunctions than the non-axisymmetric case that follows below.

The thermal condition of the upper boundary is that the heat flux is given, while the lower boundary has zero temperature perturbation (conducting lower plane). Thereby buoyancy is active near the upper plane, which means that the upper plane destabilizes the classical Horton-Rogers-Lapwood problem [1], [2]. Nield [13] investigated this destabilization due to given heat flux at the upper boundary, which reduces the critical Rayleigh number (for an unlimited horizontal layer) from its classical critical value $Ra_c = 4\pi^2$ to $Ra_c = 27.10$. Barletta *et al.* [14] computed the precise numerical values $(Ra_c, k_c) = (27.09763, 2.326215)$ for this onset problem, where k_c denotes the horizontal wave-number of the preferred mode of disturbance. Nield's results had already been confirmed by Wang [12] who solved the onset problem to a vertical cylinder with wall conditions compatible with normal-modes dependency over the circular cross-section of the cylinder.

Our numerical results for conducting wall ($a = 0$) show that the conducting outer wall tends to stabilize the porous cylinder because it gives a

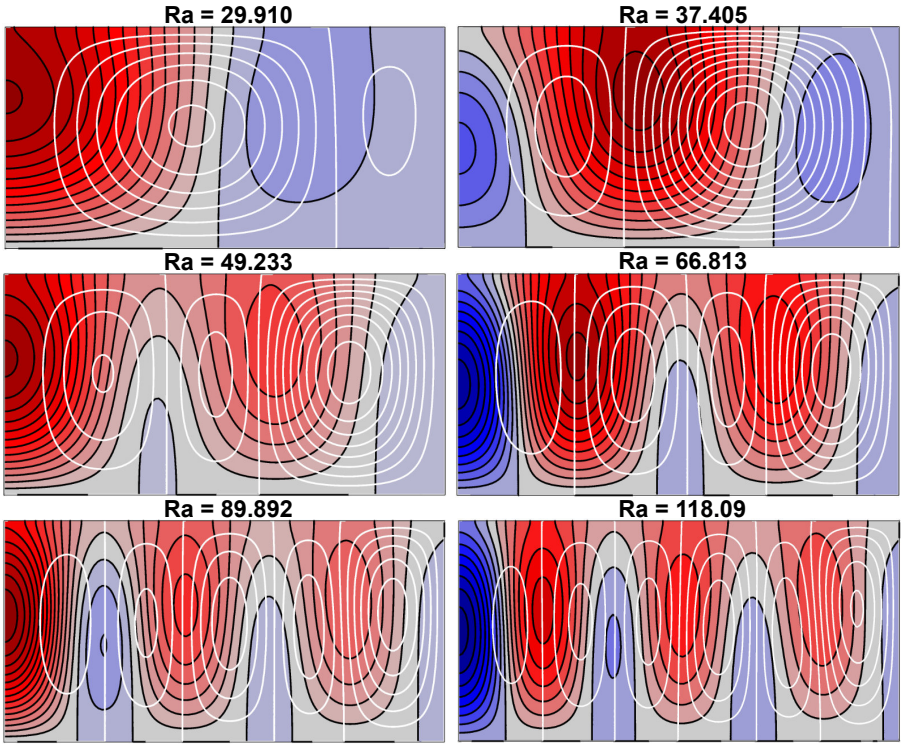

Fig. 5 Axisymmetric eigenfunction plots ($m = 0$) for a short cylinder ($R = 2$). Black lines and coloring represent isotherms, while white lines are streamlines. Conducting cylinder wall ($a = 0$).

higher critical Rayleigh number than the value $Ra_c = 27.10$, which is the asymptotic limit as $R \to \infty$ found by Nield [13]. *Figures* 3-5 give plots for the thermo-mechanical eigenfunctions for the axisymmetric case $m = 0$, representing the six eigenfunctions with the lowest Rayleigh numbers for each value of R. *Figure* 3 the eigenfunctions for a slender cylinder where $R = 0.5$. *Figure* 4 gives similar plots for a cylinder where the half cross-section is a square ($R = 1$). The short-cylinder case $R = 2$ is illustrated in *Figure* 5. We note from *Figures* 3-5 that the lowest Rayleigh number approaches Nield's asymptotic value 27.10 as R increases.

The thermo-mechanical eigenfunctions in *Figures* 3-5 are axisymmetric and include both isotherms (black lines with color marking) and streamlines (white lines). Since these are non-normal modes eigenfunctions, their spatial dependencies in the radial and vertical directions are not separable. All streamlines are confined within the impermeable boundaries. The isotherms for the temperature perturbations are perpendicular to the upper boundary, due to the constant heat flux condition there. At the three other boundaries, the isotherms are tangential to the boundaries, which is the same behavior as that of the streamlines.

There are flow cells, all of which are finite structures enclosed within the porous cylinder. Moreover, there are thermal cells, which are not necessarily closed because the isotherms are perpendicular to the upper boundary. It is important to distinguish between external cell walls and internal cell walls. The external cell walls coincide with external physical boundaries. The internal cell walls are walls between neighboring cells within the porous cylinder. Because of the spatially non-separable eigenfunctions, no internal cell walls will be exactly vertical or horizontal. These non-normal modes eigenfunctions cannot have separate mode numbers for the horizontal (radial) direction and the vertical direction, so they are ranked in the order of increasing Rayleigh numbers.

An interesting difference between axisymmetric flow patterns and their associated isotherms is the mass balance constraint which implies the existence of a vertical streamline along the cylinder axis (where $r = 0$), while the similar symmetry for the isotherms makes them horizontal instead of vertical at $r = 0$. The thermal cell walls and the flow cell walls must necessarily coincide at the cylinder wall where the isotherms and streamlines are tangential to the boundary. Thus the outer cylinder boundary serves as a thermal cell wall and a flow cell wall, in contrast to the properties of internal cell walls, where the thermal cell walls and the flow cell walls will not coincide but have mutual spatial displacement, which is well-known from eigenfunctions of normal-mode type.

Normal-mode eigenfunctions in the horizontal direction will have a quarter of a wavelength displacement between a thermal cell and a flow cell. Each flow cell has a central stagnation point, which would be located at the boundary between two neighboring thermal cells if these cells were of normal-mode type.

In *Figures* 3-5, we observe how these stagnation points are displaced away from the respective thermal cell walls, because of the non-normal modes eigenfunctions. We also note that the vertical position of the stagnation points will not be identical for two neighboring flow cells, which is an effect of non-normal modes. A cell wall for the flow is defined by a streamline connected to dividing streamlines going all the way to the outer wall. A thermal cell wall is defined by zero perturbation temperature.

When we compare the cases of increasing radii, from $R = 0.5$ in *Figure* 3 to $R = 2$ in *Figure* 5, we note that the behavior of the eigenfunctions become more similar to normal modes when R increases. When an internal thermal cell wall is farther than one length unit from the cylinder wall, we can expect that this thermal cell wall (defined by zero perturbation temperature) is located close to a stagnation point for the flow, which we will keep in mind when we turn our attention to onset modes that are not axisymmetric.

At the upper circular boundary ($z = 1, r = R$), we expect a weak singularity for the flow, somewhat similar to the 2D problem [8], but even more difficult mathematically. Near this troublesome contour circle, we observe the contrasting behaviors of the streamlines versus isotherms: (i) At the cylinder wall $r = R$ near the top (z slightly smaller than one), the streamlines are parallel to the isotherms. (ii) At the cylinder to $z = 1$ just inside the cylinder wall (R slightly smaller than R), the streamlines are perpendicular to the

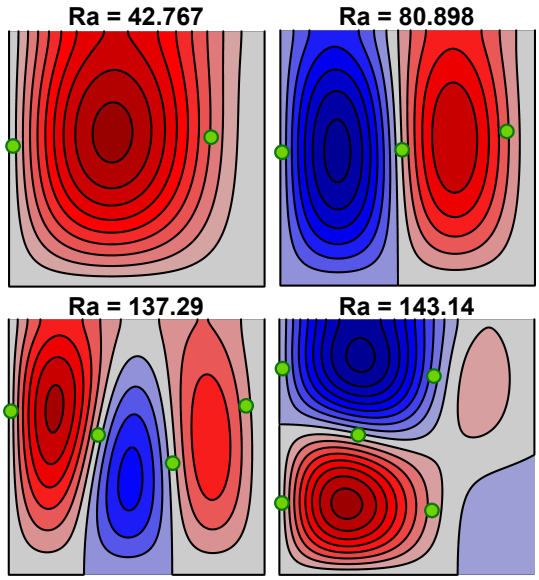

Fig. 6 Non-axisymmetric eigenfunction plots ($m = 1$) for a cylinder with dimensionless radius $R = 1$. Black lines and coloring represent isotherms, while the green dots are stagnation points for the streamlines. Conducting cylinder wall ($a = 0$).

isotherms. This contrasting behavior, as (r, z) approaches $(R, 1)$ from inside the porous cylinder, makes it impossible to derive a valid Taylor expansion around the upper corner $(r, z) = (R, 1)$ of the computational domain. This is a non-analytical corner, which is probably singular, but we will not pursue the mathematical challenges in the present work. Our numerical solution seems to work well for the outer flow (in a matched-asymptotic expansion), which indicates that singularities are weak, not affecting the Rayleigh number of the convection onset.

4.2 First azimuthal mode $m = 1$

We include one figure for the first azimuthal mode $m = 1$ where there is angular periodicity with an angle 2π of periodicity around the symmetry axis $r = 0$. This is *Figure* 6, where we have chosen the value $R = 1$ for the dimensionless cylinder radius, and we still assume that the cylinder wall is conducting ($a = 0$). The stagnation points in the vertical cross-section $OABC$ are included as green dots in *Figure* 6. We note that most of these stagnation points are fairly close to the thermal cell walls, more so than in the axisymmetric case displayed in *Figure* 5. We note the emergence of several stagnation points located at the z axis. In the case of axisymmetry, stagnation points along the symmetry axis could only occur when there were two or more flow cells in height.

The most important constraint for the non-axisymmetric temperature fields is that the perturbation temperature is zero along the cylinder axis $r = 0$.

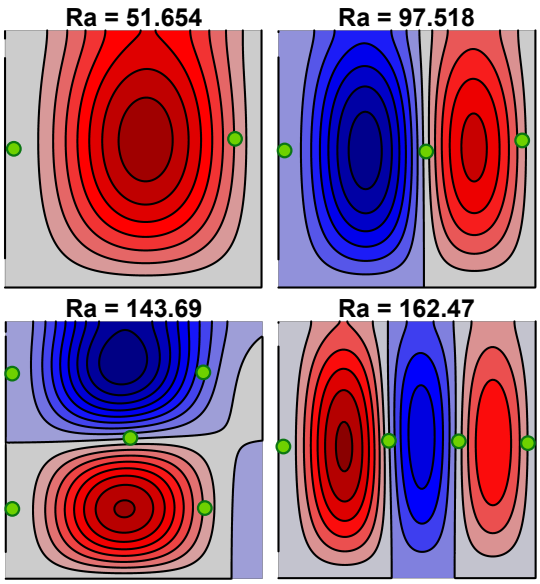

Fig. 7 Non-axisymmetric eigenfunction plots ($m = 2$) for a cylinder with dimensionless radius $R = 1$. Black lines and coloring represent isotherms, while the green dots are stagnation points for the streamlines. Conducting cylinder wall ($a = 0$).

This means that the non-axisymmetric isotherms are vertical at z axis, while we noted that the axisymmetric isotherms are horizontal at the z axis. Thus there is a great contrast between axisymmetric isotherms that are normal to the cylinder axis, while all non-axisymetric isotherms are perpendicular to the cylinder axis. We note this difference when we compare *Figure* 6 with the preceding *Figures* 3-5 representing axisymmetric non-normal modes.

Non-axisymmetric modes with the azimuthal mode number $m \geq 1$ will have m periodic cells in a horizontal plane, which requires that the z axis represents an intersection between the cell walls, and any thermal cell wall is defined by $\theta = 0$.

4.3 Second azimuthal mode $m = 2$

We also include one figure for the second azimuthal mode $m = 2$ where there is angular periodicity with an angle π of periodicity around the symmetry axis $r = 0$. This is *Figure* 7, where we chose the same dimensionless radius $R = 1$ as in *Figure* 6.

We note that the stagnation points (green dots) in *Figure* 7 are even closer to the cell walls of the thermal cells than in *Figure* 6. This has to do with the higher number ($m = 2$) of azimuthal modes, in *Figure* 7.

The lowest modes in *Figures* 6 and 7 share the property that the entire cross-section has a positive perturbation temperature, which does not happen

for axisymmetric thermal eigenfunctions. The reason that positive temperature perturbation is admissible over a cross-section is that the azimuthal periodicity (with $m \geq 1$) provides an opposite sign of the temperature half an azimuthal wavelength apart. Thus the periodicity provides a full balance between domains of hot and cold fluid in the porous medium.

4.4 The Rayleigh number as a function of the radius

In *Figures* 8 and 9, we plot the Rayleigh number at marginal stability, but it would be too much to plot all the eigenfunctions in one figure. We choose to show only the axisymmetric modes $m = 0$ in *Figure* 8, and the twelve lowest axisymmetric modes are displayed. In *Figure* 9 we show only the lowest mode (with the lowest Rayleigh number) for each azimuthal mode number m, ranging from $m = 0$ (axisymmetry) to $m = 5$. Color marking shows the domains with different values of m, and we note that the two lowest azimuthal modes $m = 0$ and $m = 1$ are the ones that represent the onset of convection, within our computed parameter range $0 < R < 4$. Table 1 shows the values (Ra, R) of the four intersection points where the preferred value of m switches back and forth between $m = 0$ and $m = 1$.

We note from *Figure* 9 that each preferred mode for the different azimuthal modes m show a Rayleigh number Ra that decreases monotonously with the radius R. As a contrast, *Figure* 8 is limited to the axisymmetric mode $m = 0$, but illustrates that the higher modes for fixed m can have a more complicated behavior.

A model which is comparable with the present one was presented by Haugen and Tyvand [11]. They considered a vertical circular cylinder with conducting walls, and the only difference from the present model was that the upper boundary was assumed to be thermally conducting. In this previous model [11], axisymmetry was always preferred, since this gave a more stable situation with no buoyancy near the symmetric lower and upper boundaries. *Figure* 9 shows that the axisymmetric mode is either preferred or gives a Rayleigh number only slightly above the overall critical Rayleigh number.

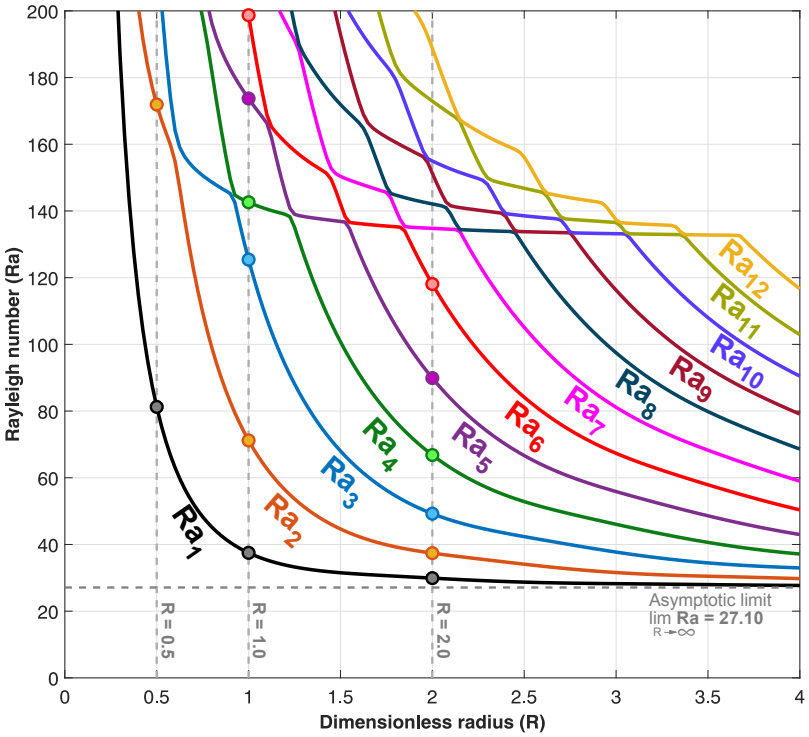

Fig. 8 Rayleigh numbers (Ra) at marginal stability as a function of dimensionless radius (R) for the 12 first eigenfunctions for $m = 0$. The filled circles refer to the cases displayed in Figs. 3, 4 and 5.

5 Numerical and analytical results for $a > 0$

So far we have made computations only for the case of a conducting cylinder wall ($a = 0$). We will now investigate the class of eigenvalue problems where the cylinder wall is partly or fully insulating ($a > 0$).

5.1 Numerical results for finite Robin parameter a

Our first computation for a partly conducting cylinder wall is shown in *Figure* 10, where we choose the value $a = 1$ for the Robin parameter. Figure 10 shows the critical Rayleigh number for the onset of convection as a function of the dimensionless radius. *Figure* 10 is analogous to *Figure* 9 (for $a = 0$), representing the lowest non-normal onset mode for each azimuthal mode number, ranging from $m = 0$ to $m = 5$. Color markings are again applied for visualizing the preferred value of m in the different intervals of the dimensionless radius R. While our computations showed that only $m = 0$ and $m = 1$ would represent the preferred onset mode when $a = 0$ (*Figure* 9), the computations for $a = 1$ (*Figure* 10) show narrow radius intervals where either $m = 2$ or

$m = 3$ gives the preferred mode of convection onset. Another interesting peculiarity of *Figure* 10 is that the onset Rayleigh numbers $Ra(R)$ for each value of m are no longer monotonously decreasing functions of R, as they are for a conducting wall (*Figure* 9).

In *Figure* 12 below, we will give more detailed numerical results for the Rayleigh number dependency of the Robin parameter a, but surprisingly we will need analytical results for interpreting *Figure* 12.

5.2 Analytical theory for the separable case $a = \infty$

The limit case of a thermally conducting cylinder wall is now solved for the purpose of benchmarking our numerical results. The case $a = \infty$ has been solved analytically by Wang [12]. This case is a 3D thermo-mechanical eigenvalue problem separable in space. Tyvand and Storesletten [4] showed that the separate 2D subproblem for the cross-section is degenerate with normal modes as solutions. We will now complement and confirm the analysis of Wang [12].

The vertical eigenvalue problem separates out, so we may write the thermal eigenfunction as $\theta = F(r, \phi)Z(z)$ to be determined by the procedure given by Barletta *et al.* [16]. The following two variables ζ and η are introduced

$$\zeta = \sqrt{k(\sqrt{Ra} + k)}, \qquad \eta = \sqrt{k(\sqrt{Ra} - k)}. \tag{42}$$

Normal modes are eigenfunctions of a Helmholtz equation, where the wave number k serves as the eigenvalue.

5.2.1 Normal modes for the circle cross-section

The horizontal eigenfunctions are expressed in polar coordinates as

$$F(r, \phi) = \mathrm{J}_m(kr)e^{im\phi}, \tag{43}$$

where J_m denotes the Bessel function of the first kind. The degenerate eigenvalue problem has the joint thermal and kinematic boundary condition

$$\left.\frac{\partial F}{\partial r}\right|_{r=R} = 0, \quad \text{implying} \quad \mathrm{J}'_m(kR) = 0. \tag{44}$$

Wooding [5] and Zebib [15] applied this boundary conditions at the cylinder wall. Thereby one introduces the sequence of wave numbers $k = k_n$ satisfying $\mathrm{J}'_m(k_n R) = 0$, ranking these wave-numbers according to increasing magnitude. Each value of the azimuthal mode number m has its own set of radial eigenvalues (wave number) which may be denoted by $k_{n,m}$.

5.2.2 1D non-normal modes for the vertical direction

In the special case, $a = \infty$, we separate out the normal-mode dependency horizontally. We are left with non-normal modes for the vertical z direction, and this 1D problem that can be solved analytically. Following Barletta *et al.* [16] we find the dispersion relation

$$\zeta \tan(\eta) + \eta \tanh(\zeta) = 0, \tag{45}$$

in agreement with Wang [12]. Each legal value of the wave number $k = k_{n,m}$ provides a set of values Ra_q for the Rayleigh number, where $q = 1, 2, ..$ represents increasing values of Ra, starting with the lowest possible value.

In *Figure* 11, we have solved the limit case $a = \infty$ numerically to provide a quite complete picture of the relationship $Ra_c(R, m)$ for the onset of convection. The critical Rayleigh number Ra_c is here represented as a function of R for all relevant azimuthal modes m. Explicit benchmarking is performed with the displayed results from Wang [12], and the agreement is excellent. Color marking is applied for visualizing the selected values of m as R varies. The different branches that are represented in Fig. 11. Each of the azimuthal modes $m = 0$, $m = 1$ and $m = 2$ refer to increasing radial modes, as specified in detail by Wang [12].

5.3 Numerical results in comparison with analytical results

Figure 11 has also been checked analytically by making new computations for $m = 0$, $m = 1$ and $m = 2$. The generalization of *Figure* 11 to the full range of values for the Robin parameter a is given in *Figure* 12. *Figure* 12 shows the critical Rayleigh number as a function of R for the following values of the Robin parameter: $a = 0$, $a = 1/3$, $a = 1$, $a = 3$, $a = \infty$. For the sake of clarity, we give separate plots for each azimuthal mode $m = 0, 1, 2, 3, 4, 5$, in *Figure* 12. For $a = \infty$ we get a slope discontinuity each time the radial mode n changes, as explained above in connection with eq. (44), and well-known from Zebib [15]. The most spectacular of these slope discontinuities is the lowest one for $m = 1$, where the critical Rayleigh number rises up to a value around 34, which gives a notable stabilization compared with the lowest value 27.10, which appears over and over again for finite values of R, each time the wavenumber k fits with the value $k = 2.33$ for an unlimited horizontal layer. We have calculated the highest point of slope discontinuity with $m = 1$, and the results are

$$R = 1.34361, \quad Ra = 34.1673, \tag{46}$$

evaluating the above analytical formulas with Mathematica. The same point has been evaluated by COMSOL Multiphysics, and the results are

$$R = 1.3434, \quad Ra = 34.1594, \tag{47}$$

which gives a satisfactory agreement.

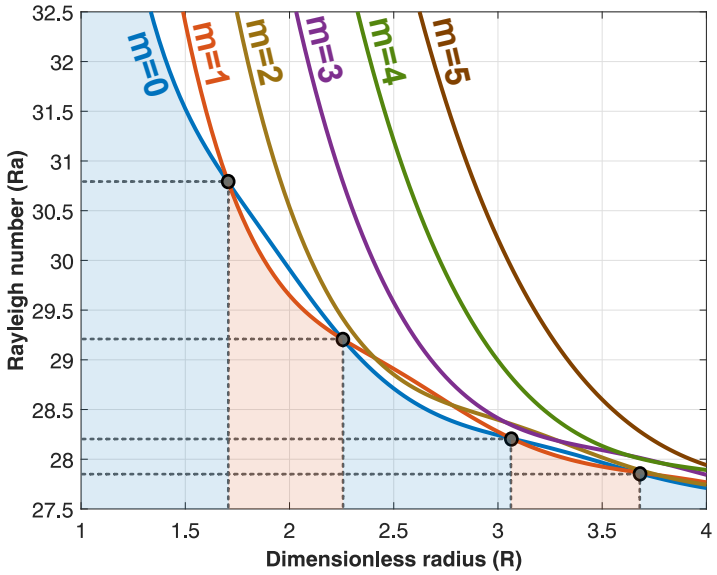

Fig. 9 The first Rayleigh number as a function of the dimensionless radius (R) for $m = 0$, $m = 1$, $m = 2$, $m = 3$ and $m = 4$, with $a = 0$.

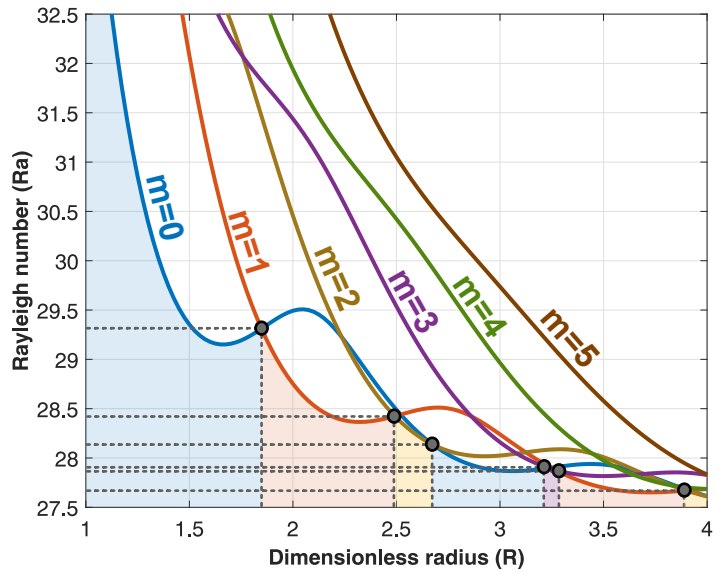

Fig. 10 The first Rayleigh number as a function of the dimensionless radius (R) for $m = 0$, $m = 1$, $m = 2$, $m = 3$, $m = 4$ and $m = 5$, with $a = 1$.

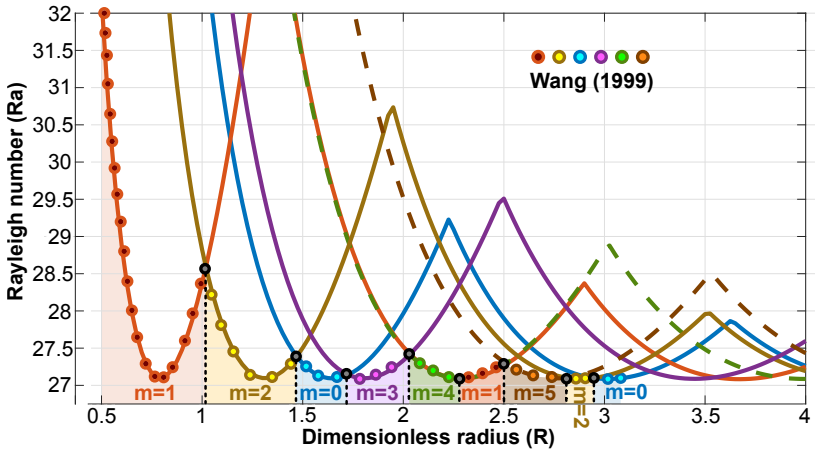

Fig. 11 The first Rayleigh number as a function of the dimensionless radius (R) for $m = 0$, $m = 1$, $m = 2$, $m = 3$, $m = 4$ and $m = 5$, with $a = \infty$. Assessment against Wang (1999).

The plots in *Figure* 12 confirm that $Ra(R)$ for $a = 0$ gives curves that are monotonously decreasing with R. However, we see the surprising result that the points of slope discontinuities for $a = \infty$ (as exemplified by eq. (46)) do not seem to change at all with varying a. This suggests a conclusion concerning the curves for $a = 0$, which is remarkable because these curves represent non-normal modes, for which no analytical methods are available: The points of slope discontinuities in the function $Ra(R)$ for $a = \infty$ provide constraints for the smooth curves $Ra(R)$ with $a = 0$. There is one particular physical reason for such a constraint: This is the requirement that any increased rate of conduction at the cylinder walls will stabilize the porous cylinder, which means that any onset curve $Ra(R, a_2)$ (with m given) must lie above a curve $Ra(R, a_1)$, if $a_2 < a_1$, and do so for any value of R. These surprising results emphasize the importance of using analytical theory, not only for benchmarking but also for interpreting results that lie outside the range of validity of analytical solution methods.

Table 1 Inter-sectional points between azimuthal mode $m = 0$ and $m = 1$ for the first eigenfunction with $a = 0$ (Points are indicated in *Figure* 9).

Description	Symbol	Intersect. 1	Intersect. 2	Intersect. 3	Intersect. 4
Rayleigh number	Ra	30.7869	29.2061	28.2061	27.8743
Dimensionless radius	R	1.7069	2.2557	3.0672	3.6525

6 On changing the thermal condition at the upper boundary

The constant-flux Neumann type thermal condition at the upper boundary $z = 1$ is responsible for the non-normal mode dependency in the vertical direction, which makes the 3D eigenvalue problem non-separable, defying analytical solutions. We will now illustrate the significance of the thermal condition at $z = 0$ by visual comparisons with the model by Haugen and Tyvand [11]. They applied the Dirichlet condition of a conducting upper boundary ($\theta|_{z=0} = 0$) to make the eigenvalue problem separable, with normal-mode dependency in the vertical direction. Thereby the 1D radial eigenvalue problem could be solved analytically in spite of being of non-normal mode type. Their model is the same as our present model with $a = 0$, except for the thermal condition at the upper boundary.

Figure 13 shows a double-cut through the porous cylinder with conducting wall $a = 0$, where the preferred axisymmetric eigenfunctions are displayed for $R = 0.5$, $R = 1$ and $R = 2$. The left-hand cross-sections represent the present problem where the upper boundary has a constant heat flux, while the right-hand cross-section represents a conducting upper boundary, studied by Haugen and Tyvand [11]. These authors did not plot streamlines, but here we can compare those streamlines and isotherms with the present model to visualize the effects of buoyancy at the upper boundary, due to the condition of given heat flux. The effects on the isotherms are obviously strongest since they meet the upper boundary perpendicularly instead of tangentially. The difference in the streamline patterns is not so easy to see, but we know that the model by Haugen and Tyvand [11] always gives internal cell walls that are horizontal or vertical, which will never be the case for non-normal modes.

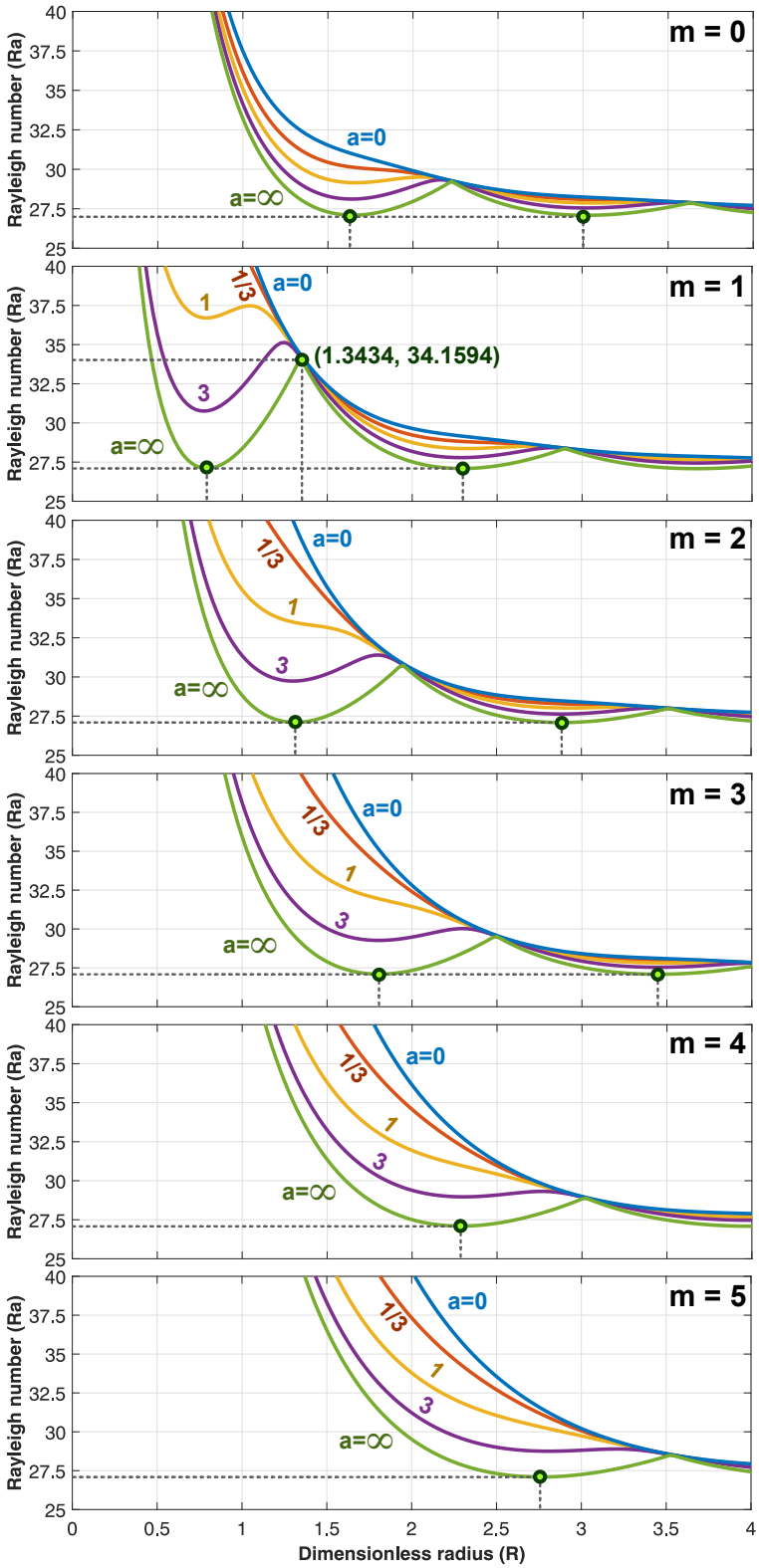

Fig. 12 The first Rayleigh number as a function of the dimensionless radius (R) for $a = 0$, $a = 1/3$, $a = 1$, $a = 3$ and $a = \infty$, with $m = 0$, $m = 1$, $m = 2$, $m = 3$, $m = 4$ and $m = 5$. Local maximum for $m = 1$ and $a = \infty$ is highlighted with coordinates. Markings of the three curves with finite values of the Robin parameter a are omitted in the upper subplot due to space limitations, but they follow the color coding of the other subplots.

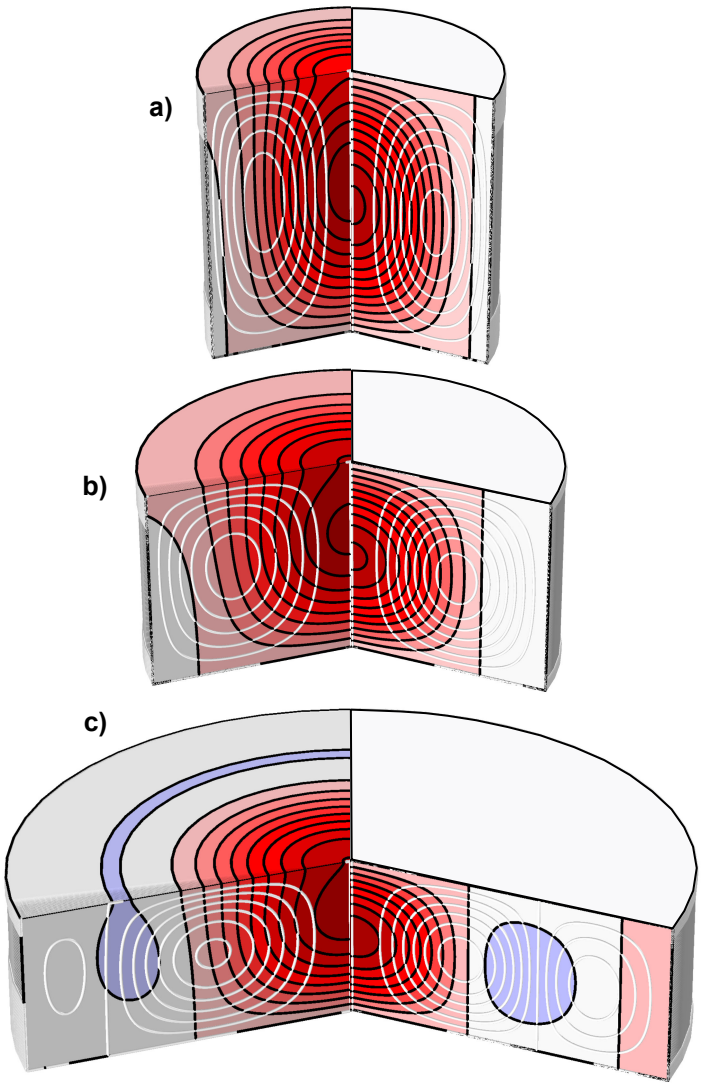

Fig. 13 Three-dimensional view of the first thermal and stream eigenfunctions for dimensional radius equal to **a)** $R = 0.5$, **b)** $R = 1$, **c)** $R = 2$. Left-hand side shows present model. Right-hand side shows the model by Haugen and Tyvand (2003) for comparison.

7 Summary and conclusions

In this contribution, we study the fourth-order Darcy-Bénard eigenvalue problem for the onset of thermal convection in a vertical porous cylinder with impermeable walls theoretically. The three-dimensional (3D) problem is analyzed numerically in a reduced two-dimensional (2D) form for the vertical r, z plane

in cylinder coordinates. A Robin-type thermal boundary condition of partial conduction is applied at the cylinder wall, introducing a as a parameter of partial conduction at the cylinder wall. The lower the value of a, the cylinder wall will become more conductive, with $a = 0$ as the limit of perfect conduction with zero perturbation temperature at the wall. The limit of insulating cylinder wall $a \to \infty$ is an important case for benchmarking our numerical results since it has an analytical solution elaborated by Wang [12].

Partial conduction at the cylinder wall is allowed in the present model. It obtains a gradual transition between the non-normal modes (with a finite) and the well-known analytical solution for $a = \infty$ [12]. Thereby, we have the opportunity of addressing an interesting question; We want to know whether a more insulating wall (implying a reduction of the parameter a) will always stabilize the physical system. The answer is yes, which is remarkable when we consider *Figure* 12 with the pronounced peaks in the dispersion relation plots in the R, Ra plane (radius versus Rayleigh number). At these sharp peaks (referring only $a = \infty$), the solution switches between two different Fourier-Bessel components in the radial direction. As a result, we have found that the points with peaks do not change with changing the parameter a, but they become smooth instead of sharp once a gets a finite value. The dispersion relation for the limit case of a conducting wall ($a = 0$) provides a monotonous curve that goes through the peaks where the analytical solution switches between two preferred modes for an insulating wall ($a = \infty$). In fact, this is a surprising effect, indicating that the pointwise switching between preferred modes for the analytical normal-mode solution (when $a = \infty$) delivers precise constraints for the non-normal mode solution, even though it cannot be found analytically.

The present work appears as a 3D version in analogy with our first paper on non-normal modes for convection in a porous rectangle [8]. Instead of a non-analytical corner of a porous rectangle in 2D, we have obtained a non-analytical circle contour for the 3D cylinder. A corner or boundary curve is called non-analytical when there exists no locally valid Taylor expansion for the thermo-mechanical eigenfunctions. There is probably a weak singularity there, but it is very challenging mathematically and is left for future work.

A weak singularity will, by definition, not affect the eigenvalue of the critical Rayleigh number. It will be governed by the outer solution in terms of a matched asymptotic expansion. This appears to be the type of solution that we have studied numerically. The present fully 3D work on non-normal modes of convection onset is a step in the direction of a physically adequate modeling that can capture the full experimental reality going beyond artificial mathematical constraints.

References

1. Horton, C.W. and Rogers, F.T. (1945) Convection currents in a porous medium. J. Appl. Phys. **16**, 367-370.
2. Lapwood, E.R. (1948) Convection of a fluid in a porous medium. Proc. Camb. Phil. Soc. **44**, 508-521.

3. Beck, J.L. (1972) Convection in a box of porous material saturated with fluid. Phys. Fluids **15**, 1377-1383.
4. Tyvand, P.A. and Storesletten, L. (2018) Degenerate onset of convection in vertical porous cylinders. J. Eng. Math. **133**, 633-651.
5. Wooding, R.A. (1959) The stability of a viscous liquid in a vertical tube containing porous material. Proc. R. Soc. Lond. **A252**, 120-134.
6. Storesletten, L. and Tveitereid, M. (1991) Natural convection in a horizontal porous cylinder. Int. J. Heat Mass Transf. 34, 1959-1968. Referred to in the text as the ST paper.
7. Rees, D.A.S. and Tyvand, P.A. (2004) The Helmholtz equation for convection in two-dimensional porous cavities with conducting boundaries. J. Eng. Math. 490, 181-193.
8. Tyvand, P.A., Nøland, J.K. and Storesletten, L. (2019) A non-normal-mode marginal state of convection in a porous rectangle. Transp. Porous Med. **128**, 633-651,
9. Barletta, A. and Storesletten, L. (2015) Onset of convection in a vertical porous cylinder with a permeable and conducting side boundary. Int. J. Therm. Sci. **97**, 9-16.
10. Nygård, H. S. and Tyvand, P.A. (2011) Onset of Thermal Convection in a Vertical Porous Cylinder with a Partly Conducting and Partly Penetrative Cylinder Wall. Transp. Porous Med. **86**, 229-241.
11. Haugen, K.B. and Tyvand, P.A. (2003) Onset of thermal convection in a vertical porous cylinder with conducting wall. Phys. Fluids **15**, 2661-2667.
12. Wang, C.Y. (1999) Thermo-convective stability of a fluid-saturated porous medium inside a cylindrical enclosure - permeable top constant flux heating. Mech. Res. Commun. **26**, 603-608.
13. Nield, D.A. (1968) Onset of thermohaline convection in a porous medium (appendix). Water Resources Res. **11**, 553-560.
14. Barletta, A., Rossi di Schio, E., Storesletten, L. (2013) Convective instability in a horizontal porous channel with permeable and conducting side boundaries. Transp. Porous Med. **99**, 515-533.
15. Zebib, A. (1978) Onset of natural convection in a cylinder of water saturated porous media. Phys. Fluids **21**, 699-700.
16. Barletta, A., Tyvand, P.A. and Nygård, H.S. (2015) Onset of convection in a porous layer with mixed boundary conditions. J. Eng. Math. **91**, 105-120.